# On the Relevance of Point Defects for the Selection of Contacting Electrodes: Ag as an Example for $Mg_2(Si,Sn)$-based Thermoelectric Generators

*Sahar Ayachi*[a], Radhika Deshpande[a], Prasanna Ponnusamy[a], Dr. Sungjin Park[b], Dr. Jaywan Chung[b], Dr. SuDong Park[b], Dr. Byungki Ryu[b], Prof. Eckhard Müller[a,c], Dr. Johannes de Boor*[a]*

a: German Aerospace Center, Institute of Materials Research, Department Of Thermoelectric Materials and Systems, Cologne, North Rhein-Westphalia, 51147, Germany

b: Energy Conversion Research Center, Electrical Materials Research Division, Korea Electrotechnology Research Institute (KERI), Changwon 51543, Korea

c: JLU Giessen, Institute of Inorganic and Analytical Chemistry, Giessen, Hessen, 35390, Germany

*Corresponding Authors: Sahar Ayachi: Sahar.ayachi@dlr.de, Johannes deBoor: Johannes.deBoor@dlr.de

**Keywords:** thermoelectrics, contacting, electrodes, defects, diffusion

https://doi.org/10.1016/j.mtphys.2020.100309

**Abstract:**

In developing thermoelectric generators, optimizing interfaces between thermoelectric materials and contacting electrodes is a crucial step. Among the tested electrodes for $Mg_2(Si,Sn)$-based generators, Ag shows good adhesion, controllable interfaces and low electrical contact resistances. However, it induces unexpected changes in the Seebeck coefficient of n-type samples, while no change is observed in p-type.

In order to understand said behavior, contacting results for Bi-doped $Mg_2Si$, $Mg_2Sn$ and $Mg_2Si_{1-x}Sn_x$ with Ag are compared with predictions based on defect formation energies obtained within hybrid-density functional theory (DFT). A qualitative description of the Ag diffusion mechanism in $Mg_2X$ is also introduced.

Calculation results show that Ag-induced defects have sufficiently low formation energies to influence charge carrier concentrations, particularly Ag substitution on the Mg site ($Ag_{Mg}$). $Ag_{Mg}$ acts as an acceptor and causes a counter-doping effect by compensating the electrons provided by Bi. However, in Li-doped p-type, as Li-defects have the lowest formation energies, a negligible charge carrier concentration change is predicted, which fits with experimental observations. Concerning solid solutions, interpolation from the binaries predicts a similar behavior, which also meets experimental findings. Therefore, this work not only establishes the calculation method and explains the observed effect, but also proves the importance of defects in selecting contacting electrodes.

## 1. Introduction

Thermoelectric (TE) materials are used in several industrial fields such as aerospace, automotive, and industry; and research to develop more environmental-friendly TE generators is continuously expanding [1-4]. In order to have a highly efficient TE device, contacting the TE legs is as important as optimizing the TE material [5, 6]. In fact, this step adds contact resistances and potential chemical interactions between the contact materials and the TE material, and both can be detrimental to the TE device if not controlled. The electrical contact resistances $R_c$, as well as the thermal contact resistances, have to be kept as low as possible, and the electrodes should be chemically and physically stable metals or conductive intermetallics that (mechanically) adhere well to the TE material [7, 8]. There should also preferably be very limited diffusion between the metal and the semiconductor that would result in reactions forming new phases. All the mentioned conditions should remain stable in the long term under working temperature and thermal stress [9]. That is also why the electrode and the TE material should have similar coefficients of thermal

expansion (CTE), which would guarantee a stable behavior free of failure under temperature cycling.

Several studies on developing contacting solutions were conducted, studying different material systems for thermoelectric applications. In fact, finding suitable contacts is a material specific problem, as the outcome will depend on the TE material, the metallic electrode and the potential interactions between them (CTE, adhesion, diffusion, reaction …). Among others, Ni [10, 11] and Fe [12] were studied with PbTe showing good bonding results thin interface layers and low electrical contact resistances, Ti [13] and Fe-Ni [14] were successfully tested for skutterudites materials, and Mo [15] and Ag [16] were used with half-heusler systems.

One of the also frequently studied TE materials are $Mg_2Si_{1-x}Sn_x$ solid solutions as they consist of abundant elements, are environmentally friendly, and have improved thermoelectric properties compared to their binaries [17-21]. Contacting of $Mg_2Si_{1-x}Sn_x$ materials was tested using Ag [22] Ni [22-24] and Cu [7, 25, 26] electrodes, and electrical contact resistances and microstructure of the reaction layers were reported.

In this work and for the first time, contacting $Mg_2Si_{1-x}Sn_x$ based-TEGs is studied from a point defect perspective. We discuss here experimental results of contacting for the binaries $Mg_2Si$ and $Mg_2Sn$ as well as the $Mg_2Si_{1-x}Sn_x$ solid solutions with Ag as a suitable example for the importance of point defects in the thermoelectric material in the selection of joining electrodes.

The issue was first observed while contacting n- and p- type $Mg_2Si_{1-x}Sn_x$ (with $x$ = 0.4 and $x$ = 0.3, respectively) with Ag, where the results showed different behaviors of the TE materials after joining [22]. In fact, not only the electrical contact resistances were very different ($r_c$ ~ 400 ± 38 μΩ cm$^2$ for n-type vs. ~ 9 ± 1 μΩ cm$^2$ for p-type, both joined at 450 °C), but also a change in the Seebeck values of the n-type samples was measured after joining (from ~ - 110 μV K$^{-1}$ to ~ - 200 μV K$^{-1}$ at room temperature), while they remained unchanged for p-type samples (~ 100 μV K$^{-1}$).

A similar behavior was also observed after contacting n- and p-type $Mg_2Si_{0.3}Sn_{0.7}$ with Cu [25]. Seebeck values of n-type samples also changed during contacting (from ~ - 110 µV $K^{-1}$ to ~ - 160 µV $K^{-1}$) and annealing (to ~ - 230 µV $K^{-1}$), while no change was observed for p-type samples. In this study, only Ag will be considered because it showed a less complex reaction layer and much less diffusion than what was observed with Cu as reported in [22] and in [25].

However, $Mg_2Si_{1-x}Sn_x$ solid solutions are known to suffer from demixing under certain conditions [27-29] and indeed demixing into Si-rich and Sn-rich phases was observed for both Cu and Ag contacted samples, potentially also influencing the Seebeck coefficient. In order to reduce the chemical complexity and identify the origin of the observed alteration of the Seebeck coefficient, we contacted n-type $Mg_2Si$ and $Mg_2Sn$ with Ag at different temperatures. To further understand the observed Seebeck behavior, an investigation of the intrinsic and extrinsic point defects of the studied binaries is required. This does not come as a surprise, as point defects are known to play a crucial role in determining semiconductors´ conduction types [30-33]. In fact, for materials like $Bi_2Te_3$, references [34, 35] reported that, under anion-rich conditions, the antisite defect Te on Bi ($Te_{Bi}$) account for the n-type conduction, while, under cation-rich conditions, the negatively charged antisite defects such as Bi on Te sites ($Bi_{Te}$) account for the p-type conduction. As for the case of $Bi_2Se_3$, the n-type conduction was related to the Se on Bi antisite defect ($Se_{Bi}$) under anion-rich conditions, while it was related to the Se vacancies ($V_{Se}$) under cation-rich growth conditions. Defect studies and computation of their formation energies can be easier done for binaries than for solid solutions, and an interpolation to the intermediate ternary compositions can be achieved from the results of the binaries. This explains why almost all respective research focuses on the binary $Mg_2X$ (X = Si, Sn, Ge) rather than to their solid solutions.

In the case of $Mg_2X$ materials, Kato *et al.* [36] used density-functional theory (DFT) calculations to evaluate point defect formation energies in $Mg_2Si$ and to understand the origin of the previously reported intrinsic n-type conduction of this material [37, 38] Their results showed that the n-type conduction comes from the positively charged ($q$ = 2+) Mg ions at interstitial sites ($I_{Mg}$), which are the most energetically stable point defects under both Mg-rich and Mg-poor (Si-rich) conditions.

Jund *et al.* [39] studied the relative stabilities of $Mg_2Si$ and $Mg_2Ge$ using first principles calculations with different functionals. They showed that the stability of the point defects strongly depends on the growth conditions. In case of $Mg_2Si$, under stoichiometric and Mg rich conditions, Mg interstitials ($I_{Mg}$) is the most stable defect, while under Mg poor conditions, $Si_{Mg}$ is more stable. This contradicts what was reported by Kato [36], but Kato *et al.* considered charged defects and dependence of the formation energies on chemical potentials, while Jund *et al.* considered neutral defects.

Another work by Liu *et al.* [40] stated that Mg vacancies $V_{Mg}$ and Mg interstitials $I_{Mg}$ are the dominant defects in $Mg_2Si$ and $Mg_2Sn$, independently of the chemical environment (Mg-rich or Si/Sn-rich). The concentration of these defects is what determines the conduction type in each material. $V_{Mg}$ is an acceptor ($q$ = 2-) more favorable under Mg-depleted conditions, and $I_{Mg}$ is a donor more favorable under Mg-rich conditions. Si/Sn related defects are less likely to occur in the binaries, partly because their ionic radii (2.72 Å / 2.94 Å) are larger than that of Mg (0.66 Å), so the local disorder and strain due to these defects are much larger than the strain caused by Mg related defects.

Meanwhile, there have been few studies on intrinsic defects in $Mg_2Sn$ mitigated by the band gap underestimation in conventional DFT calculations, i.e. using the local density approximation or generalized gradient approximation. While Liu *et al.* [40] reported a quantitative analysis of the possible intrinsic defects in $Mg_2Si$, $Mg_2Ge$, and $Mg_2Sn$, their quantitative analysis of the defect

densities suffers from a severe band gap underestimation: most of the major carriers are compensated by the minority carriers due to the small band gap calculated by DFT. This underestimation of the band gap persists with other works using conventional DFT, including the works of Kato *et al.* [36] and Jund *et al.* [39] mentioned above. In agreement with this, our conventional DFT calculations also showed that the band gap is obtained negative for $Mg_2Sn$. Such band gap underestimations affect the electronic chemical potential, which in turn affects defect stabilities. To overcome this issue, advanced computational methods such as hybrid-DFT [41] and quasi-particle calculations [42] were found to be important. Our recent hybrid functional study on intrinsic defects in $Mg_2Si$ and $Mg_2Sn$ finally quantitatively describes the intrinsic defect properties of these material systems [43].

Besides intrinsic defects, extrinsic defects (e.g. due to doping) are used to tune the carrier concentration of TE materials as the most common way to improve *zT* [44-47]. As these "added" defects can be more stable than the intrinsic defects of the material and influence the charge carrier concentrations in the chemical potential region of interest, both defect types need to be taken into consideration in order to have a full picture and predict the materials´ behavior [48].

The aim of this paper is to understand the unexpected behavior of Ag contacted n-type $Mg_2Si_{1-x}Sn_x$ using first principle calculations of point defect formation energies. In order to model the experimental situation (doped $Mg_2X$ in contact with Ag), we investigate the simultaneous presence of intrinsic and extrinsic defects in n- and p-type $Mg_2Si$ and $Mg_2Sn$ employing hybrid DFT calculations [41].

An understanding for the solid solutions can then be extrapolated. The considered dopants for n- and p- type conductions are respectively Bi and Li, and both Mg-rich (for n-type) and Mg-poor (for p-type) conditions are discussed.

Our findings show that the extrinsic defects generated after joining Ag with $Mg_2Si_{1-x}Sn_x$, namely $Ag_{Mg}$, are behind the experimentally observed Seebeck changes in n-type materials. $Ag_{Mg}$ acts as an electron trap for the conduction electrons provided by Bi ($Bi_{Si}$ for $Mg_2Si$ and $Bi_{Sn}$ for $Mg_2Sn$), leading to a decrease in the majority charge carrier density. In case of p-type materials, Ag related defects have higher formation energies than Li defects, which makes the influence of $Ag_{Mg}$ or $I_{Ag}$ not as visible as in n-type materials.

This example highlights that, in thermoelectricity, defect calculations are not just important for TE material development and dopant selection, but they also need to be taken into consideration when selecting contacting electrodes.

## 2. Material and methods

### 2.1. Sample Preparation and Characterization

$Mg_2Si$ and $Mg_2Sn$ were prepared from ball milled powder as reported in [18] with the respective nominal stoichiometries $Mg_{2.06}Si_{0.97}Bi_{0.03}$ and $Mg_{2.15}Sn_{0.97}Bi_{0.03}$. The powders from each material were pressed into three 15 mm diameter pellets for 10 min, at 800 °C for $Mg_2Si$ and at 600 °C for $Mg_2Sn$ [49] in a direct sinter press and then joined with Ag foil. The contacting experiments were also done through current assisted joining in the same direct sinter press. Each pellet was joined at a different temperature: 450, 500 and 550 °C for $Mg_2Si$, and 400, 450 and 500 °C for $Mg_2Sn$. The heating rate was 1 K $s^{-1}$ and the holding time was 10 min for each sample. These temperatures were selected because 450 °C showed to be a good joining temperature for $Mg_2Si_{1-x}Sn_x$ [22].

The solid solution $Mg_2Si_{1-x}Sn_x$ samples were prepared with the following stoichiometry: $Mg_{2.06}Si_{0.3}Sn_{0.665}Bi_{0.035}$ for n-type and $Mg_{1.98}Li_{0.02}Si_{0.4}Sn_{0.6}$ for p-type according to the procedures reported in [22], [25] and [50]. Three extra samples were prepared for this particular study following the procedure described in [22] to further investigate the observed trends: the first of

these samples was prepared using 5 g of n-type $Mg_2Si_{0.3}Sn_{0.7}$ powder instead of the usual 1.2 g, which was then pressed in a 15 mm diameter pellet (700 °C, 20 min) and contacted with Ag foil at 450 °C for 10 min. The second and the third samples were made out of pre-pressed n- and p-type pellets that were joined together with Ag foils in between, also at 450 °C for 10 min. These samples were joined in two different experiments, one where the n-type pellet was at the bottom and the p-type pellet was on top of the Ag foil (referred to as *n//Ag//p*) and one where the stacking order was reversed (*p//Ag//n*).

Property characterization of the samples was done with SEM/EDX for microstructure investigations along the cross sections, and with an in-house built Potential & Seebeck Scanning Microprobe (PSM) [23, 51] for Seebeck measurements. Estimations of carrier concentration $n$ and reduced chemical potential $\eta$ were obtained from experimental results of the Seebeck coefficient combined with the effective mass ($m^*_D$) values from a single parabolic band (SPB) model based on the following equations [19, 52-54]

$$S = \frac{k_B}{e}\left(\frac{2F_1(\eta)}{F_0(\eta)} - \eta\right) \quad (1)$$

$$n = 4\pi\left(\frac{2m_D^* k_{b_B} T}{h^2}\right)^{1.5} F_{\frac{1}{2}}(\eta) \quad (2)$$

where $k_B$ is Boltzmann´s constant and $F_i(\eta)$ is the Fermi integral of order $i$.

### 2.2. Hybrid-DFT Calculations for Defect Formation Energies

First-principles calculations were performed to investigate the electrical properties of intrinsic and extrinsic defects in $Mg_2Si$ and $Mg_2Sn$ within the hybrid-DFT calculations [55] using the Vienna Ab Initio Simulation Package [56, 57]. The hybrid exchange-correlation energy function of HSE06 was employed with the exact-exchange mixing parameter of 25% and the screening parameter of

0.208 Å$^{-1}$. The planewave energy basis set was used with the energy cutoff of 296 eV. The projector-augmented wave pseudopotentials were used for atomic potentials.

To model the defective system, a (2×2×2) cubic supercell was used with the lattice parameters of 6.35 Å and 6.75 Å for $Mg_2Si$ and $Mg_2Sn$, respectively. In the supercell, there are 64 Mg and 32 Si/Sn atoms, and the dopant atom is added, removed, or replaced in the host supercell to generate defective supercells for vacancy, substitutional, and interstitial defects. The Γ-centered (2×2×2) *k*-point mesh was sampled for charge density integration over the Brillouin zone. The atomic positions were fully relaxed until the magnitude of the remaining forces was smaller than 0.005 eV Å$^{-1}$.

The charged defect formation energy of a defect *D* in the charge state *q* ($D^q$) in the $Mg_2X$ was obtained using the following equation

$$E_{\mathrm{form}}(D^q, \mathrm{Mg_2X}) = E_{\mathrm{tot}}[D^q] - E_0 - \Sigma_j\left(\mu_j \Delta n_j\right) + q(E_{\mathrm{F}} + E_{\mathrm{CBM}})$$

where $E_{tot}[D^q]$ and $E_0$ are the total energies with and without defect in the supercell, *j* is the atomic species in the supercell, $\Delta n_j$ is the number change of atomic species *j* in the defective supercell with respect to the pristine supercell without defects, $E_F$ is the electron Fermi level, and $E_{CBM}$ is the energy of the conduction band minimum (CBM) [43, 58, 59]. Note that for the defects, the total energies were calculated using HSE06. However due to the huge computational cost, the spin-orbit interaction is not included.

## 3. Results

### 3.1. $Mg_2Si/Sn$ with Ag

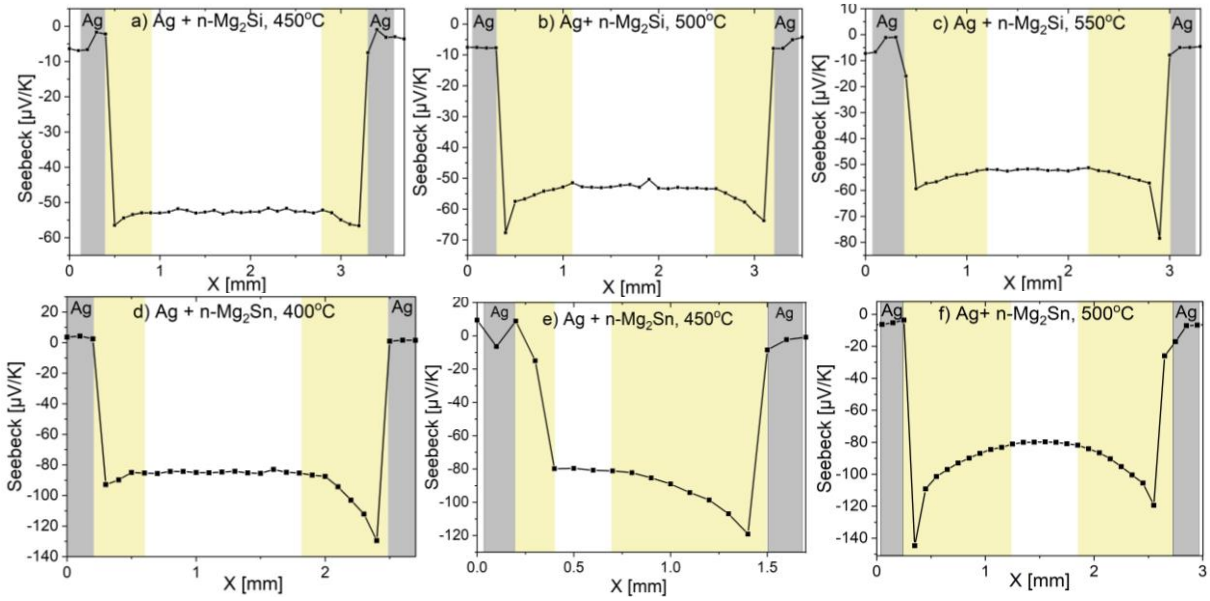


***Figure 1:*** *Representative Seebeck profiles for $Mg_2Si$ and $Mg_2Sn$ contacted with Ag at different temperatures. The grey rectangles indicate the Ag foil and the yellow rectangles delimit the length where the Seebeck coefficient is altered. (Color should be used in print).*

Seebeck scan lines by the PSM at room temperature of n-$Mg_2Si$ and n-$Mg_2Sn$ joined with Ag at 3 different temperatures, (450 °C, 500 °C, 550 °C) and (400 °C, 450 °C, 500 °C) respectively, are presented in **Figure 1**. All the samples displayed an interesting Seebeck profile where the *S* values peak near the interfaces and then return back to the bulk value beyond a certain depth. The portions of the samples where S changed are marked with yellow rectangles on **Figure 1**. As no significant local variation was observed in the samples before the joining step, it must be linked to the interaction with the electrode. The observed changes in the Seebeck coefficient are believed to be caused by the diffusion of Ag into the TE material. For each binary, the diffusion of Ag, observed by the zone width of the altered Seebeck coefficient, differs with temperatures as can be seen in **Figure 1**. The presented line scans of the Seebeck coefficient are representative of the general behavior for each sample.

The average change in Seebeck coefficient in the $Mg_2Si$ samples is comparable for all joining temperatures. The Seebeck value of the bulk of the TE material is maintained around -55 µV $K^{-1}$ for all samples, and the average values close to the interface are -57 ± 1 µV $K^{-1}$, -63 ± 10 µV $K^{-1}$ and -58 ± 2 µV $K^{-1}$ respectively for 450 °C, 500 °C and 550 °C. The high standard deviation observed for the sample joined at 500 °C comes from the line to line scatter, potentially due to local inhomogeneities in the sample. Moreover, while the maximum drop of the Seebeck coefficient recorded for 450 and 550 °C were respectively -65 µV $K^{-1}$ and -81 µV $K^{-1}$, it locally reached -115 µV $K^{-1}$ for 500 °C.

The $Mg_2Sn$ samples showed a similar Seebeck gradient behavior, but unlike for the $Mg_2Si$ samples, we consistently observed differences between the two contacting interfaces. As can be seen from **Figure 1**, $Mg_2Sn$ joined at 400 and 450 °C exhibit steep drops on the one side, but almost no drop on the other. Whether this is due to the electromigration of Ag during the current-assisted joining or due to different reaction layers on both sides cannot be clearly stated. Interestingly, in the case of the sample joined at 500 °C, both sides have similar average Seebeck behavior. Even though the graph shown in **Figure 1** f) displays an uneven (local) situation, line to line variation averages both sides to similar values. Averages of the Seebeck values near the interfaces and their corresponding estimated carrier concentrations for both $Mg_2Si$ and $Mg_2Sn$ are provided in **Table S 1** in the Supplementary Material.

Another difference which can be observed in the samples depending on the joining temperature is the increase of the width of the layer where *S* is different from bulk values (interior of the TE material). In the case of $Mg_2Si$ samples, while this layer has a length of only 0.3 mm for $T_{join}$ = 450 °C, it increases to 0.6 mm for $T_{join}$ = 500 °C and 0.8 mm for $T_{join}$ = 550 °C.

To have a better description of Ag diffusion inside $Mg_2X$ systems as well as gain an understanding of the dependence of this diffusion on temperature, a simple exponential decay function (Equation 1) was used to fit the experimental results and quantify the observed changes:

$$S(x) = S_{bulk} + A\exp(\frac{-x}{\tau}) \quad (3)$$

where $S_{bulk}$ is the Seebeck of the TE material, $A$ is the amplitude and $\tau$ the effective diffusion length. As each Seebeck line scan contains two graded sections opposite in decay direction, each line scan was divided into two fits: the first fit was the right-hand side gradient to which Equation 1 was applied as is, while the second fit was the left-hand side gradient which was first mirrored then fitted to the same equation. The fitting results are presented in **Table 1** and divided as described into left and right sides. A verification of this model based on the fitting with Equation 3 is provided in section I of the Supplementary Material. A good agreement between the modelling and the experimental data can be deduced from Figure S1 of the Supplementary Material.

**Table 1***: Fitting results of the diffusion length $\tau$ and the amplitude A from Seebeck line scans of $Mg_2Si$ and $Mg_2Sn$. $S_{inter}$ is the result of Equation 3 at the interface and $n_{inter}$ the corresponding carrier concentration obtained using Equations 1 and 2 and the constants reported in [19] and [18]. Bulk values before contacting are S = 55 μV K$^{-1}$, n = 2.5 × 10$^{20}$ cm$^{-3}$ for $Mg_2Si$ and S = 80 μV K$^{-1}$, n = 3 × 10$^{20}$ cm$^{-3}$ for $Mg_2Sn$*

| | $T_{join}$ – side | $\tau$ [mm] | $A$ [μV K$^{-1}$] | $S_{inter}$ [μV K$^{-1}$] | $n_{inter}$ ($10^{20} \times$ cm$^{-3}$) |
|---|---|---|---|---|---|
| $Mg_2Si$ | 450 – Left side | 0.13 | 3.4 | 58 | 2.4 |
| | 450 – Right side | 0.09 | 6.2 | 61 | 2.2 |
| | 500 – Left side | 0.19 | 10 | 65 | 2.0 |
| | 500 – Right side | 0.15 | 22.5 | 78 | 1.5 |
| | 550 – Left side | 0.28 | 8.1 | 63 | 2.1 |
| | 550 – Right side | 0.38 | 9.9 | 65 | 2 |
| $Mg_2Sn$ | 400 – Left side | 0.11 | 12 | 92 | 2.8 |
| | 400 – Right side | 0.15 | 32 | 112 | 2.1 |
| | 450 – Left side | – | – | – | – |
| | 450 – Right side | 0.24 | 45.5 | 125 | 1.6 |
| | 500 – Left side | 0.22 | 42.2 | 122 | 1.7 |
| | 500 – Right side | 0.17 | 46.4 | 127 | 1.5 |

**Table 1** shows that the diffusion of Ag in $Mg_2Si$ at each temperature has comparable diffusion lengths $\tau$ and amplitudes $A$ on both contacted sides. The table also shows an overall increase of $\tau$ and $A$ with temperature.

As for $Mg_2Sn$ samples, the difference in amplitude originates from the difference in interface Seebeck coefficient values between both sides of each sample, particularly those joined at 400 and 450 °C. The left side of the 450 °C sample was omitted because there was no $S$ gradient. $\tau$ values do not show a clear temperature dependence like in $Mg_2Si$, as a deeper diffusion is seen at 450 °C, though just on one side.

The obtained values of $\tau$ and $A$ were implemented in Equation 1, and values of $S(x)$ and corresponding carrier concentrations $n$ at the interface were also reported in **Table 1**. The latter were estimated using Equations 1 and 2, assuming $m_D^* = 1.1\ m_0$ [60] and $m_D^* = 2\ m_0$ [61].

Using the obtained values of $\tau$, diffusion coefficients and activation energies were calculated. Using $\tau = \sqrt{Dt}$ where $\tau$ is the diffusion length (mm), $D$ is the diffusion coefficient ($m^2\ s^{-1}$) and $t$ is the diffusion time (s), we can estimate the diffusion coefficient $D(T)$ for each joining temperature using averaged values of $\tau$ from both sides as given in **Table 1** and $t$ = 600 s as the holding contacting time. The temperature-independent proportionality constant $D_0$ ($m^2\ s^{-1}$) and the activation energy $E_A$ (J $mol^{-1}$) are obtained from fitting the Arrhenius equation $D(T) = D_0 \exp(-\frac{E_A}{RT_{join}})$ [62]. In this equation, the molar gas constant $R$ is fixed at 8.314 J $mol^{-1}$ $K^{-1}$ and $T$ is the absolute temperature (K).

Here, we only present results for $Mg_2Si$, as they display a systematic behavior with temperature, unlike $Mg_2Sn$. The obtained values of $E_A$ and $D_0$ were respectively 111 kJ $mol^{-1}$ = 1.15 eV and 1.8

$\times 10^{-3}$ $m^2$ $s^{-1}$. They were both extracted from the slope and the intercept of the fitting line to the Arrhenius plot presented in ***Figure 2***.

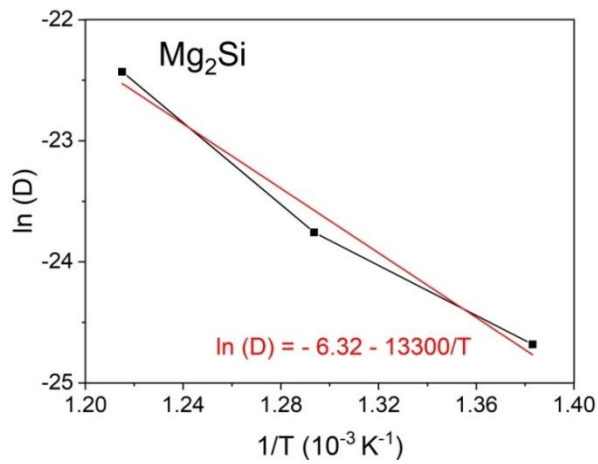


***Figure 2****: Arrhenius plot of the diffusion constant of Ag in $Mg_2Si$*

### 3.2. $Mg_2Si_{1-x}Sn_x$ with Ag

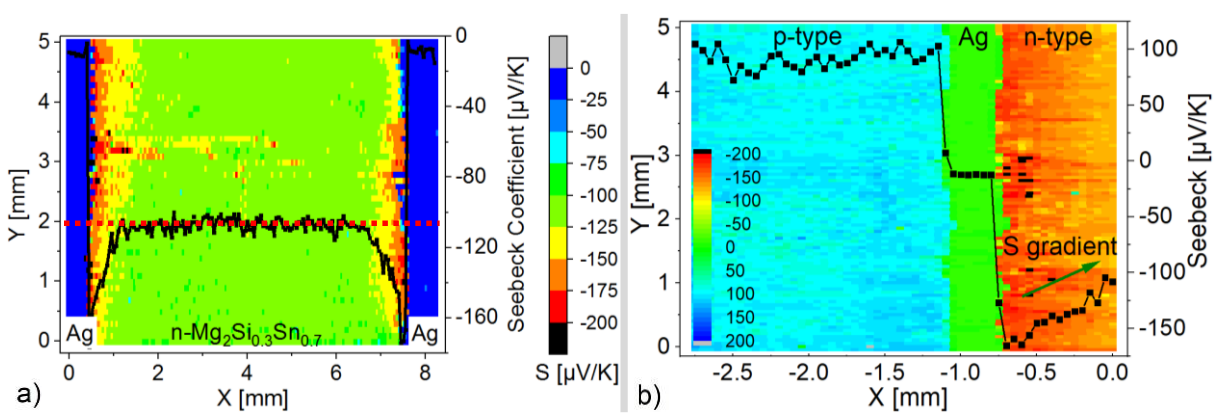


***Figure 3****: Exemplary Seebeck profile scans and 2D surface plots of a) thick n-type $Mg_2Si_{0.3}Sn_{0.7}$ joined with Ag at 450 °C, and b) simultaneously joined p-type (bottom), Ag (middle) and n-type (top) materials displaying a Seebeck gradient only for the n-type. The selected Seebeck profile line scans correspond to the scan positions y = 0.6 mm and y = 5 mm for a) and b) respectively. (Color should be used in print).*

After confirming the change of Seebeck behavior during contacting on the $Mg_2Si$ and $Mg_2Sn$ binaries, further experiments on the solid solution were conducted. Unlike the previously reported case with thin samples where *S* changed along the whole sample thickness [22], the thick n-type $Mg_2Si_{0.3}Sn_{0.7}$ sample presented in this work showed a seemingly different behavior after joining. In fact, as shown in **Figure 3** (a), *S* value changes occurred near the interfaces only, reaching $S_{max}$ ~ -170 μV $K^{-1}$, which is qualitatively similar to what was observed for the binaries. This change of Seebeck corresponds to a change in carrier concentration from $n = 2.9 \times 10^{20}$ $cm^{-3}$ to $n = 1.18 \times 10^{20}$ $cm^{-3}$ assuming $m_D^* = 2.5\ m_0$ [17]. It is clear through the line scan as well as the 2D plot in **Figure 3** (a) that there is a gradient of the Seebeck near the electrodes, but that *S* values go back to the bulk value (~ -110 μV $K^{-1}$, marked with the red dashed line) after a depth of ~ 0.75 mm on each side. Taking this depth into account, the results of the thick sample are not inconsistent with those of the previously reported thin samples, because the thin samples have a thickness of ~ 1.5 mm, which is completely covered by the actual depth of the gradient zones on both sides.

The same fitting procedure (Equation 1) used for the binaries was also applied here, and an average value for the diffusion length $\tau(T_{join})$ from both joining interfaces was obtained. The obtained values are $\tau(T_{join})$ = 0.38 mm and $D(T_{join}) = 2.4 \times 10^{-10}$ $m^2$ $s^{-1}$. These numbers are closer to those obtained for $Mg_2Sn$ at 450 °C / 723 K ($9.6 \times 10^{-11}$ $m^2$ $s^{-1}$) than those for $Mg_2Si$ ($1.9 \times 10^{-11}$ $m^2$ $s^{-1}$), which is not surprising as the used ternary is rich in $Mg_2Sn$ (~ 70%).

The simultaneously joined n- and p- type stacked samples were produced by joining pre-pressed n- and p- pellets with Ag foil in between. No Ag foil was added on the external sides of the pellets. The purpose of this experiment was to investigate a simultaneous diffusion/electromigration of Ag, and to rule out preparation and technical uncertainties. Seebeck scans of the *p//Ag//n* sample were collected and are presented in **Figure 3** (b), while results for the *n//Ag//p* sample are provided in the Supplementary Material (**Figure S 2**).

As shown in the 2D plots in **Figure 3** (b), a Seebeck gradient is only visible in the n-type side of the stacked sample, while no such gradient was observed in p-type. Similar results were observed in the second stacked sample (n//Ag//p) where, the change in *S* was again only recorded in the n-type pellet (stacked at the bottom of the sample arrangement). This shows that the Ag diffusion has a stronger and more visible effect in n-type, and that it is mainly not driven by current (electromigration). Instead, it is driven by temperature, and the extent of the diffusion and its effects seem to depend on the dominant carrier type.

## 4. Discussion

The observed behavior might in principle and qualitatively be explained by Ag-induced point defects in the thermoelectric material. The formation energy of charged defects is a function of the Fermi level and will thus differ between n and p-type counterparts of the "same" composition, potentially leading to different abundance of defects in the n and p-type materials. The lattice diffusion process is governed by the diffusion barrier of the relevant defect, which is the sum of its formation energy and its migration barrier [63], and is therefore also dependent on the Fermi level of the electrons. For example, as negatively charged defects have lower formation energies in n-type than in p-type, they will be more abundant, and more mobile in n-type than in p-type. Based on our experimental results, we thus speculate that negatively charged acceptor-like defects will be generated during contacting the TE legs, affecting the charge carrier concentration and the Seebeck coefficient. To substantiate this hypothesis, calculations of the formation energies of these defects are performed for the binaries $Mg_2Si$ and $Mg_2Sn$. This also establishes a base for interpolation to interpret the result for the ternary combinations.

**Figure 4** shows the calculated formation energy curves of the relevant intrinsic and extrinsic defects in n-and p-type $Mg_2Si$ and $Mg_2Sn$ doped with Bi and Li, respectively, and contacted with

Ag. Defects related to Bi and Li were considered as dopants for $Mg_2Si$ and $Mg_2Sn$, while Ag point defects were considered to understand the possible influence of the electrode on the thermoelectric materials. In both material cases, the conduction band minimum (CBM) is fixed at $E$ = 0 eV. So, using the calculated values of the band gaps from hybrid-DFT, we obtained the positions of the valence band maxima (VBM) for $Mg_2Si$ and $Mg_2Sn$ as 0.570 eV and 0.145 eV. These values are comparable to the experimental band gaps which are 0.77 and 0.35 eV, respectively [64]. Note that within conventional DFT calculations using local-density approximation and GGA, the band gaps are severely underestimated to be ~ 0.2 eV and ~ -0.19 eV for $Mg_2Si$ and $Mg_2Sn$, respectively [41], and the defect stability could be improperly described.

As n-type samples are made with 3 at% excess Mg, we might suppose that they are under Mg-rich chemical potential conditions. However, Mg losses are expected to occur during the initial pellet pressing step and then the joining step. Even though these losses are not straightforward to quantify, we also consider Mg-poor conditions for n-type $Mg_2Si$ and $Mg_2Sn$. In **Figure 4**, only the relevant defects with formation energies lower than 1 eV are presented. Full figures with complete formation energies under all conditions are provided in the Supplementary Material, with **Figure S 3** and **Figure S 4** representing all the defects in $Mg_2Si$ and $Mg_2Sn$, respectively.

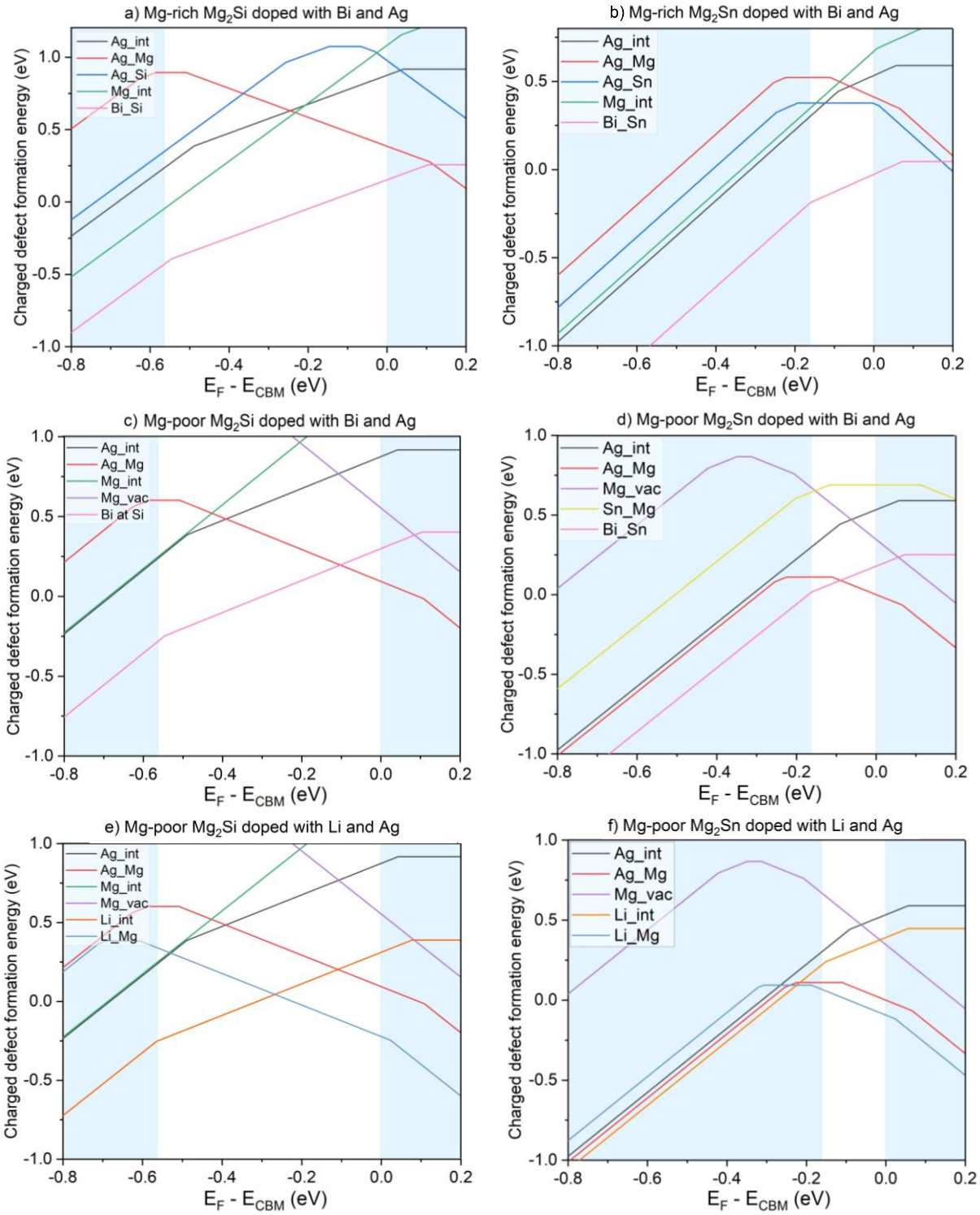


***Figure 4****: Formation energy curves for a) Bi- and Ag-related defects in Mg-rich $Mg_2Si$, b) Bi- and Ag-related defects in Mg-rich $Mg_2Sn$, c) Bi- and Ag-related defects in Mg-poor $Mg_2Si$, d) Bi- and Ag-related defects in Mg-poor $Mg_2Sn$, e) Li- and Ag-related defects in Mg-poor $Mg_2Si$ and f) Li- and Ag-related defects in Mg-poor $Mg_2Sn$. $E_F$ is given with respect to the conduction band maximum, and the white regions indicate the band gaps. (Color should be used in print).*

In n-type $Mg_2Si$ on **Figure 4** (a), $Bi_{Si}$ becomes the most stable defect with the lowest formation energy. It is a shallow donor defect with the charge state of $q$ = 1+ for both low and high doped $Mg_2Si$ (up to $E_F$ = 0.1 eV, which is where the Fermi level can be pinned). It is also more stable than $I_{Mg}$ which is the main (intrinsic) defect behind the n-type conduction in non-doped $Mg_2Si$. Such observation can be underpinned by experimental findings showing that the tuning range of the carrier concentration with extrinsic dopants is wider than by just adjusting Mg content. Kato *et al*.[36], in fact, demonstrated that they could tune the carrier concentration by less than $1 \times 10^{20}$ $cm^{-3}$ with changing Mg content, while they could reach $1 \sim 2 \times 10^{20}$ $cm^{-3}$ through Bi or Sb doping. Under Mg-poor conditions, as displayed on **Figure 4** (c), $Bi_{Si}$ is also the most stable defect, however only for a smaller chemical potential range than Mg-rich conditions. In fact, the pinned Fermi level $E_F$ is at -0.1 eV, if Ag point defects are considered. However, if we disregard the Ag defects potentially generated due to the contacting electrode, $Bi_{Si}$ would be the most stable defect up until a chemical potential of 0.1 eV.

For the n-type samples, the chemical potential for the electrons is $E_F \sim 0$ eV. Under both (Mg) chemical potential conditions, the second defect of interest is $Ag_{Mg}$, a shallow acceptor defect with $q$ = 1-. As shown in **Figure 4** (a) and (c), in the range of $E_F$ = -0.5 to 0.1 eV, $Bi_{Si}$ and $Ag_{Mg}$ have opposite charges, as the former is a 1+ donor and the latter is a 1- acceptor. These two most stable defects will then compensate, which causes a decrease in the charge carrier concentration in the n-type material. With increasing $E_F$, the defect density of $Ag_{Mg}^{1-}$ increases, and at a certain energy, $Ag_{Mg}^{1-}$ can be the major defect. Note also that the $Ag_{Mg}$ defect formation energy becomes lower when the Mg atomic chemical potential changes from Mg-rich to Mg-poor.

Considering the defect density equation $n\,(D,q) = N_0 e^{-\frac{E_{form}(D,q)}{k_B T}}$, where $N_0$ is the total density of possible sites that can form a defect $D$ at charge state $q$ [65], $n\,(D,q)$ of a defect decreases quickly with increasing formation energy $E_{form}(D,q)$. Therefore, the compensation effect of $Bi_{Si}^{1+}$

by $Ag_{Mg}^{1-}$ is more visible when the formation energies of both defects are either close or when $E_{form}(Ag_{Mg}) < E_{form}(Bi_{Si})$. Our experimental samples are heavily doped, with $E_F \sim 1\ k_BT \sim 0.026$ eV. Around this chemical potential, $E_{form}$ of $Ag_{Mg}$ and $Bi_{Si}$ are comparable, so the charge compensation effect would be detectable, which matches the experimental data. For lower Fermi level samples, the difference in formation energy between the two defects increases, corresponding to a smaller expected compensation.

Using the method of climbed nudged elastic band (cNEB) calculations [59, 66, 67], we reveal that Ag defects in $Mg_2Si$ can easily diffuse to form $Ag_{Mg}$ defects via the interstitial diffusion of the $I_{Ag}$ interstitial defect with a migration energy barrier of 0.652 eV. When the Fermi level is 0 (i.e. $E_F = E_{CBM}$), as the formation energies of $I_{Ag}^{1+}$ are 0.88 and 0.53 eV in Mg-rich $Mg_2Si$ and $Mg_2Sn$ respectively, the diffusion barrier will be in the range of 1.2 – 1.5 eV. When the diffused $I_{Ag}$ is split into $Ag_{Mg}$ (electron trap) and $I_{Mg}^{2+}$ (donor), and the separated $I_{Mg}^{2+}$ defect diffuses far away (e.g. to grain boundary or electrode), the remaining $Ag_{Mg}$ defect will finally act as the electron trap and is the source of charge compensation. In the previous study, we showed that Mg diffuses easily in $Mg_2Si$ via the interstitial position [43].

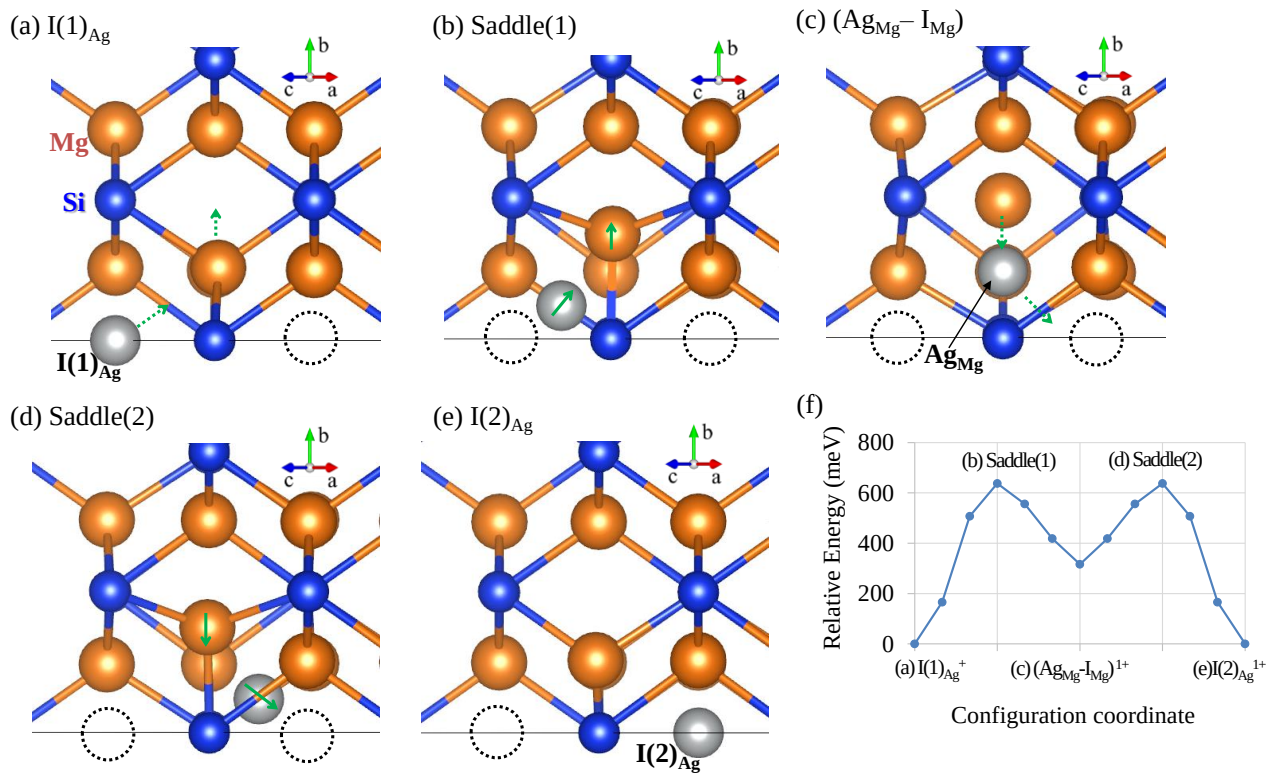


***Figure 5**: Suggested diffusion mechanism of Ag in $Mg_2Si$. The individual steps are presented in (a)-(e). The calculated relative energies of configuration coordinates during Ag diffusion are given in (f). (Color should be used in print).*

**Figure 5** (a), (b), (c), (d) and (e) shows the atomic configurations during the Ag diffusion. For the interstitial diffusion of $I_{Mg}$, we consider the initial configuration of the $I_{Ag}^{1+}$ defect in $Mg_2Si$ (**Figure 5** (a)) and the intermediate configuration of the defect complex of $(Ag_{Mg}—I_{Mg})^{1+}$ (**Figure 5** (c)). The defect $I_{Ag}$ can be transformed into an $Ag_{Mg}$ and an $I_{Mg}$ defect. In this step-1, the $I_{Ag}$ defect moves toward an Mg site to form $Ag_{Mg}$. At the same time, the pushed Mg atom moves to one of the adjacent interstitial sites to form $I_{Mg}$. These diffusion steps are described by the saddle 1 presented in **Figure 5** (b). **Figure 5** (f) shows the relative energy between the configurations during the diffusion path. Note that the energy for the intermediate state of $(Ag_{Mg}—I_{Mg})^{1+}$ is higher by 0.359 eV than that for the initial configuration state of $I_{Ag}^{1+}$, and the migration energy barrier of the "*saddle 1*" step is found to be 0.652 eV. After this step-1 ((**Figure 5** (a), (b) and (c)), the ($Ag_{Mg}$-

$I_{Mg})^{1-}$ defect cluster can be transformed again into a single $I_{Ag}^{1+}$ defect at an adjacent interstitial position. The Mg at the interstitial site can push the Ag atom at the Mg site ("*saddle 2*", (**Figure 5** (d)), and then the pushed $Ag_{Mg}$ moves to one of the adjacent interstitial sites (**Figure 5**(e)). Thus, $Ag_{Mg}$ and $I_{Mg}$ can be combined into a single $I_{Ag}$ interstitial defect: we call this step-2. This step is the exothermic reaction with the energy difference of 359 meV with a migration energy barrier of 293 meV. Note that the exothermic reaction step-2 is the reverse process of step-1. Depending on the diffusion path, the $I_{Ag}$ can be located at the original interstitial site or at a next lattice interstitial site via combination of step-1 and step 2. Thus, with multiple repetitions of step-1 and step-2, the Ag defect can easily diffuse throughout the $Mg_2Si$ in the form of $I_{Ag}^{1+}$. During the diffusion of $I_{Ag}^{1+}$, the decomposed defect of $I_{Mg}^{2+}$ can separately diffuse back into the electrode region. Then the remaining $Ag_{Mg}^{1-}$ defects can cause the charge compensation of electron carriers which were donated by Bi donors.

From the charged defect formation energies, we found that when $E_F$ is at the CBM, the defect formation energy of $I_{Ag}$ is ranging between 0.88 and 0.53 eV in $Mg_2Si$ and $Mg_2Sn$. Therefore, the diffusion barrier, the sum of the defect formation energy and the migration energy barrier, is calculated to be 1.2-1.5 eV, which is comparable to the activation energy of 1.15 eV reported in section 2.1.

From the defect density equation given above, an increase in $T$ leads to an increase of defect density. Consequently, Ag related defects are expected to be higher in number as $T$ increases, and so is the compensation effect. The number of Bi-related defects on the other hand, most likely doesn´t increase with temperature, as there is no source for new Bi incorporation and the defect configuration is frozen after material synthesis. However, a quantitative comparison between the experimental results and the predictions by DFT are difficult as, first, the carrier concentrations are

also affected by the (unknown) Mg content/Mg chemical potential in the samples and second, we are clearly not in an equilibrium situation.

In n-type $Mg_2Sn$, as presented in **Figure 4** (b), $Bi_{Sn}$ is the most energetically stable defect. Similar to $Bi_{Si}$, it is a single shallow donor. The defects with the next lowest formation energies are $Ag_{Sn}$ and $Ag_{Mg}$. However, in the chemical potential range of $E_F$ = -0.2 ~ 0 eV ($E_{CBM}$), $Ag_{Sn}$ is a neutral defect ($q$ = 0) and therefore doesn´t affect charge carrier concentration. $Ag_{Mg}$ is a single acceptor, which basically compensates the carriers provided by $Bi_{Sn}$, just like it did for $Mg_2Si$.

These observations complete the experimental results discussed in the previous section, where a change in the Seebeck values of both binaries was observed near the contacting interfaces. We also conclude that a similar behavior can be expected for $Mg_2Si$ and $Mg_2Sn$ n-type solid solutions. In all cases, $Ag_{Mg}$ defects are expected to trap conduction electrons provided by $Bi_{Si/Sn}$, leading to a depletion of carrier concentration. Such results are detected experimentally as an increase of the Seebeck values (in absolute value), which fits with the experimental results of **Figure 3** and explains the findings of previous reports [22] and [25].

**Figure 4** (e) and (f) show the defect formation energies for $Mg_2Si$ and $Mg_2Sn$ doped with Li and Ag under Mg-poor conditions, as p-type samples are synthesized with Li substituting Mg. It is worth noticing on **Figure 4** (e) that the Fermi level in $Mg_2Si$ is pinned deep inside the band gap, which explains the experimental challenges in making good p-type $Mg_2Si$ [19, 65]. For $Mg_2Sn$, Li doping can induce p-type conduction under Mg-poor conditions due to the narrow band gap, while Li hardly gives p-type characteristics under Mg-rich conditions (see Supplementary Material).

In contrast to Ag defects in n-type $Mg_2Si/Sn$, the Ag related defects in p-type $Mg_2Si/Sn$ doped with Li have much higher formation energies than major Li defects. This means that the addition of Ag doesn´t influence the p-type conduction determined by Li defects.

As for p-type $Mg_2Si_{1-x}Sn_x$ studied here and in [22], a behavior similar to $Mg_2Sn$ is expected, as the samples are $Mg_2Sn$ rich (70 and 60%). Li-related defects are expected to be the most stable, and Ag-related defects to have high enough formation energies so that no doping effect would be experimentally detectable in a Seebeck mapping, as is experimentally observed. Similarly, the hybrid-DFT calculation results confirm that, for $Mg_2Si_{1-x}Sn_x$, Li is a better p-type dopant than Ag. In such analysis, it is important to keep in mind potential interactions between the electrode and the TE material, as well as the resulting interfaces between them. In our case, the actual diffusion process of Ag is presumably more complex than considered here. As shown in [22], Ag and $Mg_2$(Si,Sn) are practically not in direct contact but are separated by an Ag containing intermetallic layer. This, as well as potential other diffusion paths inside the thermoelectric material, will influence the diffusion of Ag, and a microscopic model is required to analyze this in depth. Nevertheless, the Seebeck coefficient profile predicted based on our simple diffusion model shows good agreement with the actual experimental *S(x)*, as shown in **Figure S 1** of the Supplementary Material. Thus, due to the good qualitative and quantitative agreement between experiment and calculation in our work, we believe our effective model provides valuable insight.

Technologically, it is also important to keep in mind that Ag diffusing into the n-type $Mg_2Si_{1-x}Sn_x$ causes a loss of major charge carriers; hence the functional material does not possess its optimum thermoelectric properties anymore, which leads to the degradation of the TE device. To illustrate this, a comparison between the properties of $Mg_2Si_{1-x}Sn_x$ before and after joining is presented.

To calculate $zT$ and the efficiency of the pristine sample (before contacting), electrical resistivity and thermal conductivity, $\rho$ and $\kappa$, data was taken from previous measurements [18]. For contacted samples, properties as observed at the interface were assumed for the whole sample, taking the interface properties as hypothetical equilibrium state after Ag saturation. As local experimental measurements of the conductivities were unfeasible and using a simple SPB model to approximate

carrier concentration from $S$ then approximating $\rho$ and $\kappa$ does not hold at high temperatures (contribution of minority charge carriers becomes substantial), the needed thermoelectric properties were taken from literature which provides a full TE study of a sample with similar $S$ as observed at the interface of **Figure 3** [68]. Therefore, the following calculations are rough estimations due to certain differences between the literature and our current work (synthesis method, dopant…). However, these effects are expected to be minor and the general trend in $zT$ and efficiency is believed to be similar. More details about the calculation and approximation procedures are provided in section III in the Supplementary Material.

The initial TE material is synthesized and doped to have optimum carrier concentration which guarantees maximum $zT$. Any loss of majority charge carriers caused by Ag diffusion, for example, results in a decrease in $zT$ as schematically shown in **Figure 6**.

Simulation results also show that, for an $Mg_2Si_{1-x}Sn_x$ leg of 5 mm length with a hot side temperature of 700 K and a cold side temperature of 300 K, the loss of carriers corresponds to a decrease of maximum efficiency from 10.5% to 7.2% and of maximum power output from 0.028 to 0.013 × $10^6$ W $m^{-2}$. Further decrease in these values is expected to occur as Ag continues diffusing inside the TE material and might alter its TE properties further beyond what we assumed to be the equilibrium state. This also establishes the importance of defect consideration in contacting electrode selection and module building.

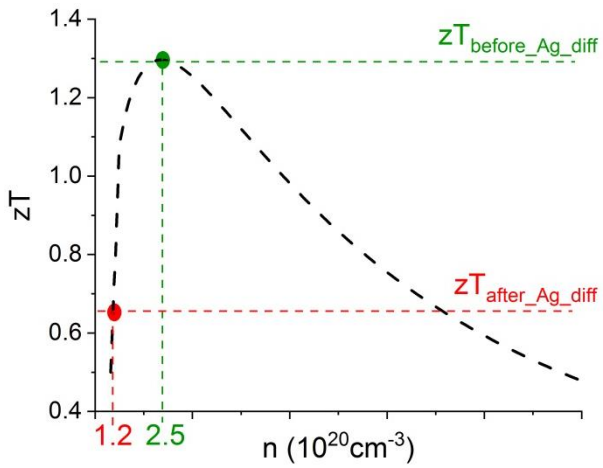


***Figure 6**: Schematic dependence of zT on carrier concentration for n-type $Mg_2Si_{1-x}Sn_x$ before and after Ag diffusion at T = 700K.*

## 5. Conclusion

In this work, we re-assess the selection of Ag as a contacting solution for $Mg_2Si_{1-x}Sn_x$-based thermoelectric generators by describing the Ag diffusion mechanism and correlating unexpected experimental results with hybrid-DFT defect calculations. The observed change in Seebeck values of n-type binaries $Mg_2Si$, $Mg_2Sn$ and their solid solutions is explained by $Ag_{Mg}$ defects which have low enough formation energy to counteract Bi-related defects and cause a diminution in charge carrier concentration. This qualitative agreement between experiments and calculations establishes the credibility of both methods, as well as the importance of a potential doping effect of the contacting electrode. Thus, we clearly show that, Ag is not a suitable electrode for n-type $Mg_2X$ without further technological steps (e.g. diffusion barriers).

Furthermore, we show that the intrinsic and extrinsic defects of the considered TE material and the joining material are important criteria to consider while screening for contacting electrodes.

**CRediT authorship contribution statement**

**Sahar Ayachi:** Methodology, Validation, Formal analysis, Investigation, Writing - original draft, Visualization.

**Radhika Deshpande:** Validation, Investigation.

**Prasanna Ponnusamy:** Software, Validation.

**Sungjin Park**: Software, Validation, Formal analysis, Investigation (theoretical).

**Jaywan Chung:** Software.

**Sudong Park:** Software, Validation, Writing - review & editing, Supervision, Funding acquisition.

**Byungki Ryu:** Conceptualization, Methodology, Software, Validation, Formal analysis, Investigation (theoretical), Writing – original draft, Project administration, Funding acquisition.

**Eckhard Müller:** Writing - review & editing, Supervision.

**Johannes de Boor:** Conceptualization, Methodology, Writing - review & editing, Supervision, Project administration.

**Declaration of competing interest**

The authors declare that they have no known competing financial interests or personal relationships that could have appeared to influence the work reported in this paper.

**Acknowledgements**

The authors would like to gratefully acknowledge the endorsement for the DLR executive Board Members for Space Research and Technology, as well as the financial support from the Young Research Group Leader Program. We would also like to thank Pawel Ziolkowski and Przemyslaw Blaschkewitz for their help and assistance with the thermoelectric measurements.

This work was also supported by the Korea Institute of Energy Technology Evaluation and Planning (KETEP) funded by the Ministry of Trade, Industry & Energy (MOTIE), Republic of Korea: Grant No. 20172010000830. The authors from the Korea Electrotechnology Research Institute (KERI) were also supported by the Korea Electrotechnology Research Institute (KERI) Primary Research Program through the National Research Council of Science and Technology (NST) funded by the Ministry of Science and ICT (MSIT) of the Republic of Korea: Grant No. 20A01025.

J. de Boor also acknowledges support by the Deutsche Forschungsgemeinschaft (DFG, German Research Foundation) - project number 396709363.

Received: ((will be filled in by the editorial staff))
Revised: ((will be filled in by the editorial staff))
Published online: ((will be filled in by the editorial staff))

**Data Availability Statement:**

The raw/processed data required to reproduce these findings cannot be shared at this time due to legal or ethical reasons.

References:

[1] L.E. Bell, Cooling, heating, generating power, and recovering waste heat with thermoelectric systems, Science 321(5895) (2008) 1457-1461. https://doi.org/10.1126/science.1158899.
[2] T.M. Tritt, Thermoelectric phenomena, materials, and applications, Annual review of materials research 41 (2011) 433-448. https://doi.org/10.1146/annurev-matsci-062910-100453.
[3] F.J. DiSalvo, Thermoelectric cooling and power generation, Science 285(5428) (1999) 703-706. https://doi.org/10.1126/science.285.5428.703.
[4] R. Santos, S.A. Yamini, S.X. Dou, Recent progress in magnesium-based thermoelectric materials, J. Mater. Chem. A 6 (2018) 3328-3341. https://doi.org/10.1039/C7TA10415D.
[5] G. Min, D. Rowe, Optimisation of thermoelectric module geometry for 'waste heat'electric power generation, J. Power Sources. 38 (1992) 253-259. https://doi.org/10.1016/0378-7753(92)80114-Q.
[6] I. Atassi, E. Bauer, J. Nicolics, B. Dangl, L. Spendlhofer, D. Knospe, F. Faistauer, Current thermoelectric materials and an evaluation of thermoelectric materials contacting approaches, 2012 35th International Spring Seminar on Electronics Technology, IEEE (2012) 70-75.
[7] L. Cai, P. Li, P. Wang, Q. Luo, P. Zhai, Q. Zhang, Duration of Thermal Stability and Mechanical Properties of $Mg_2Si$/Cu Thermoelectric Joints, J. Electron. Mater. 47 (2018) 2591-2599. https://doi.org/10.1109/ISSE.2012.6273111.
[8] G. Min, D. Rowe, O. Assis, S. Williams, Determining the electrical and thermal contact resistance of a thermoelectric module, Proc. ICT (1992) 210-212.
[9] S. Ganeshan, S. Shang, Y. Wang, Z.-K. Liu, Temperature dependent elastic coefficients of $Mg_2X$ (X= Si, Ge, Sn, Pb) compounds from first-principles calculations, J. Alloys. Comp. 498 (2010) 191-198. https://doi.org/10.1016/j.jallcom.2010.03.153
[10] X.R. Ferreres, A. Gazder, A. Manettas, S. Aminorroaya Yamini, Solid-state bonding of bulk PbTe to nickel electrode for thermoelectric modules, ACS Appl. Energy Mater. 1 (2018) 348-354. https://doi.org/10.1021/acsaem.7b00010
[11] X.R. Ferreres, S.A. Yamini, M. Nancarrow, C. Zhang, One-step bonding of Ni electrode to n-type PbTe—A step towards fabrication of thermoelectric generators, Mater. & Design. 107 (2016) 90-97. https://doi.org/10.1016/j.matdes.2016.06.038
[12] A. Singh, S. Bhattacharya, C. Thinaharan, D. Aswal, S. Gupta, J. V. Yakhmi, K. Bhanumurthy, Development of low resistance electrical contacts for thermoelectric devices based on n-type PbTe and p-type TAGS-85 ($(AgSbTe_2)_{0.15}(GeTe)_{0.85}$), J. Phys. D: Appl. Phys. 42 (2009) 015502. https://doi.org/10.1088/0022-3727/42/1/015502.
[13] D. Zhao, H. Geng, L. Chen, Microstructure contact studies for skutterudite thermoelectric devices, Int. J. Appl. Cerma. Technol. 9 (2012) 733-741. https://doi.org/10.1111/j.1744-7402.2011.02703.x
[14] S.H. Park, Y. Jin, J. Cha, K. Hong, Y. Kim, H. Yoon, C-Y. Yoo, I. Chung, High-power-density skutterudite-based thermoelectric modules with ultralow contact resistivity using Fe–Ni metallization layers, ACS Appl. Energy Mater. 1 (2018) 1603-1611. https://doi.org/10.1021/acsaem.8b00064
[15] J. Shen, Z. Wang, J. Chu, S. Bai, X. Zhao, L. Chen, T. Zhu, Low contact resistivity and interfacial behavior of p-type NbFeSb/Mo thermoelectric junction, ACS Appl. Mater. Interfaces 11 (2019) 14182-14190. https://doi.org/10.1021/acsami.9b02124
[16] P.H. Ngan, N. Van Nong, B. Balke, L. Han, E.M.J. Hedegaard, S. Linderoth, N. Pryds, On the challenges of reducing contact resistances in thermoelectric generators based on half-Heusler alloys, J. Electron. Mater. 45 (2015) 594-601. https://doi.org/10.1007/s11664-015-4156-z.

[17] N. Farahi, S. Prabhudev, G.A. Botton, J.R. Salvador, H. Kleinke, Nano-and microstructure engineering: an effective method for creating high efficiency magnesium silicide based thermoelectrics, ACS Appl. Mater. Interfaces 8 (2016) 34431-34437. https://doi.org/10.1021/acsami.6b12297.
[18] A. Sankhla, A. Patil, H. Kamila, M. Yasseri, N. Farahi, E. Mueller, J. de Boor, Mechanical alloying of optimized $Mg_2$(Si, Sn) solid solutions: understanding phase evolution and tuning synthesis parameters for thermoelectric applications, ACS Appl. Energy Mater. 1 (2018) 531-542. https://doi.org/10.1021/acsaem.7b00128.
[19] H. Kamila, P. Sahu, A. Sankhla, M. Yasseri, H.-N. Pham, T. Dasgupta, E. Mueller, J. de Boor, Analyzing transport properties of p-type $Mg_2Si$–$Mg_2Sn$ solid solutions: optimization of thermoelectric performance and insight into the electronic band structure, J. Mater. Chem. A 7 (2019) 1045-1054. https://doi.org/10.1039/C8TA08920E.
[20] V. Zaitsev, M. Fedorov, E. Gurieva, I. Eremin, P. Konstantinov, A.Y. Samunin, M. Vedernikov, Highly effective $Mg_2Si_{1-x}Sn_x$ thermoelectrics, Phys. Rev. B 74 (2006) 045207. https://doi.org/10.1103/PhysRevB.74.045207.
[21] M.I. Fedorov, V.K. Zaitsev, G.N. Isachenko, High effective thermoelectrics based on the $Mg_2Si$-$Mg_2Sn$ solid solution, Solid State Phenom.: Trans Tech Publ. 170 (2011) 286-292. https://doi.org/10.4028/www.scientific.net/SSP.170.286.
[22] N.H. Pham, N. Farahi, H. Kamila, A. Sankhla, S. Ayachi, E. Müller, J. de Boor, Ni and Ag electrodes for magnesium silicide based thermoelectric generators, Mater. Today Energy 11 (2019) 97-105. https://doi.org/10.1016/j.mtener.2018.10.016.
[23] J. de Boor, C. Gloanec, H. Kolb, R. Sottong, P. Ziolkowski, E. Müller, Fabrication and characterization of nickel contacts for magnesium silicide based thermoelectric generators, J. Alloys Compd. 632 (2015) 348-353. https://doi.org/10.1016/j.jallcom.2015.01.149.
[24] J. de Boor, D. Droste, C. Schneider, J. Janek, E. Mueller, Thermal stability of magnesium silicide/nickel contacts, J. Electron. Mater. 45 (2016) 5313-5320. https://doi.org/10.1007/s11664-016-4716-x.
[25] S. Ayachi, G. Castillo Hernandez, N.H. Pham, N. Farahi, E. Müller, J. de Boor, Interfaces, Developing Contacting Solutions for $Mg_2Si_{1-x}Sn_x$-Based Thermoelectric Generators: Cu and $Ni_{45}Cu_{55}$ as Potential Contacting Electrodes, ACS Appl. Mater. Interfaces, 11 (2019) 40769. https://doi.org/10.1021/acsami.9b12474.
[26] S. Ayachi, G.C. Hernandez, E. Müller, J. de Boor, Contacting Cu Electrodes to $Mg_2Si_{0.3}Sn_{0.7}$: Direct vs. Indirect Resistive Heating, Semiconductors 53 (2019) 1825-1830. https://doi.org/10.1134/S1063782619130025.
[27] M. Yasseri, A. Sankhla, H. Kamila, R. Orenstein, D.N. Truong, N. Farahi, J. de Boor, E. Mueller, Solid solution formation in $Mg_2$(Si, Sn) and shape of the miscibility gap, Acta Mater. 185 (2020) 80-88. https://doi.org/10.1016/j.actamat.2019.11.054.
[28] R. Viennois, C. Colinet, P. Jund, J.-C. Tédenac, Phase stability of ternary antifluorite type compounds in the quasi-binary systems $Mg_2X$–$Mg_2Y$ (X, Y= Si, Ge, Sn) via ab-initio calculations, Intermetallics 31 (2012) 145-151. https://doi.org/10.1016/j.intermet.2012.06.016.
[29] A. Kozlov, J. Gröbner, R. Schmid-Fetzer, Phase formation in Mg–Sn–Si and Mg–Sn–Si–Ca alloys, J. Alloy Compd. 509 (2011) 3326-3337. https://doi.org/10.1016/j.jallcom.2010.12.052.
[30] H.J. Queisser, E. E. Haller, Defects in semiconductors: some fatal, some vital, Science 281 (1998) 945-950. https://doi.org/10.1126/science.281.5379.945.
[31] L. Liu, Z. Mei, A. Tang, A. Azarov, A. Kuznetsov, Q.-K. Xue, X. Du, Oxygen vacancies: The origin of n-type conductivity in ZnO, Phys. Rev. B 93 (2016) 235305. https://doi.org/10.1103/PhysRevB.93.235305.

[32] S. Chen, J.-H. Yang, X.-G. Gong, A. Walsh, S.-H Wei, Intrinsic point defects and complexes in the quaternary kesterite semiconductor $Cu_2ZnSnS_4$, Phys. Rev. B 81 (2010) 245204. https://doi.org/10.1103/PhysRevB.81.245204.
[33] Z. Sun, Y. Pan, J. Zhou, B. Sa, R. Ahuja, Origin of p-type conductivity in layered *n*GeTe.*m* $Sb_2Te_3$ chalcogenide semiconductors, Phys. Rev. B 83 (2011) 113201. https://doi.org/10.1103/PhysRevB.83.113201.
[34] D. West, Y. Sun, H. Wang, J. Bang, S. Zhang, Native defects in second-generation topological insulators: effect of spin-orbit interaction $Bi_2Se_3$, Phys. Rev. B 86 (2012) 121201. https://doi.org/10.1103/PhysRevB.86.121201.
[35] J. Horák, Z. Stary, P. Lošťák, J. Pancíř, Anti-site defects in n-$Bi_2Se_3$ crystals, J. Phys. Chem. Solids 51 (1990) 1353-1360. https://doi.org/10.1016/0022-3697(90)90017-A.
[36] A. Kato, T. Yagi, N. Fukusako, First-principles studies of intrinsic point defects in magnesium silicide, J. Phys.: Condens. Matter 21 (2009) 205801. https://doi.org/10.1088/0953-8984/21/20/205801.
[37] R.G. Morris, R. Redin, G.C. Danielson, Semiconducting properties of $Mg_2Si$ single crystals, Phys. Rev. 109 (1958) 1909. https://doi.org/10.1103/PhysRev.109.1909.
[38] M. Yoshinaga, T. Iida, M. Noda, T. Endo, T. Takanashi, Bulk crystal growth of $Mg_2Si$ by the vertical Bridgman method, Thin Solid Films 461 (2004) 86-89. https://doi.org/10.1016/j.tsf.2004.02.072.
[39] P. Jund, R. Viennois, C. Colinet, G. Hug, M. Fèvre, J-C. Tedenac, Lattice stability and formation energies of intrinsic defects in $Mg_2Si$ and $Mg_2Ge$ via first principles simulations, J. Phys.: Condens. Matter 25 (2012) 035403. https://doi.org/10.1088/0953-8984/25/3/035403.
[40] X. Liu, L. Xi, W. Qiu, J. Yang, T. Zhu, X. Zhao, W. Zhang, Significant roles of intrinsic point defects in $Mg_2X$ (X= Si, Ge, Sn) thermoelectric materials, Ad. Electron Mater. 2 (2016) 1500284. https://doi.org/10.1002/aelm.201500284.
[41] B. Ryu, S. Park, E.-A. Choi, J. de Boor, P. Ziolkowski, J. Chung, S.D. Park, Hybrid-Functional and Quasi-Particle Calculations of Band Structures of $Mg_2Si$, $Mg_2Ge$, and $Mg_2Sn$, J. Korean Phys. Soc. 75 (2019) 144-152. https://doi.org/10.3938/jkps.75.144.
[42] F. Aryasetiawan, O. Gunnarsson, The GW method, Rep. Prog. Phys. 61 (1998) 237.
[43] B. Ryu, E. Choi, S. Park, J. Chung, J. de Boor, P. Ziolkowski, E. Müller, S. Park, Native point defects and low p-doping efficiency in $Mg_2$(Si,Sn) solid solutions: A hybrid-density functional study, J. Alloys Compd. 853, 157145 (2021). https://doi.org/10.1016/j.jallcom.2020.157145.
[44] S.-M. Choi, T.H. An, W.-S. Seo, C. Park, I.-H. Kim, S.-U. Kim, Doping effects on thermoelectric properties in the $Mg_2Sn$ system, J. Electron. Mater, 41 (2012) 1071-1076. https://doi.org/10.1007/s11664-012-1985-x.
[45] Z. Du, T. Zhu, X. Zhao, Enhanced thermoelectric properties of $Mg_2Si_{0.58}Sn_{0.42}$ compounds by Bi doping, Mater. Lett. 66 (2012) 76-78. https://doi.org/10.1016/j.matlet.2011.08.031.
[46] I. Aoyama, H. Kaibe, L. Rauscher, T. Kanda, M. Mukoujima, S. Sano, T. Tsuji, Doping effects on thermoelectric properties of higher manganese silicides (HMSs, $MnSi_{1.74}$) and characterization of thermoelectric generating module using p-type (Al, Ge and Mo)-doped HMSs and n-type $Mg_2Si_{0.4}Sn_{0.6}$ legs, Jpn. J. Appl. Phys. 44 (2005) 4275. https://doi.org/10.1143/JJAP.44.4275.
[47] X. Chen, A. Weathers, D. Salta, L. Zhang, J. Zhou, J.B. Goodenough, L. Shi, Effects of (Al, Ge) double doping on the thermoelectric properties of higher manganese silicides, J. Appl. Phys. 114 (2013) 173705. https://doi.org/10.1063/1.4828731.
[48] P. Gorai, V. Stevanović, E.S. Toberer, Computationally guided discovery of thermoelectric materials, Nat. Rev. Mater. 2 (2017) 17053. https://doi.org/10.1038/natrevmats.2017.53.

[49] H. Kamila, M. Yasseri, N. Pham, N. Farahi, E. Müller, J. de Boor, Synthesis of p-type $Mg_2Si_{1-x}Sn_x$ with x= 0-1 and optimization of the synthesis parameters, Mater. Today: Proc. 8 (2019) 546-555. https://doi.org/10.1016/j.matpr.2019.02.052.
[50] N. Farahi, C. Stiewe, D.N. Truong, J. de Boor, E. Müller, High efficiency $Mg_2$(Si, Sn)-based thermoelectric materials: scale-up synthesis, functional homogeneity, and thermal stability. RSC Adv. 9 (2019) 23021-23028. https://doi.org/10.1039/C9RA04800F.
[51] D. Platzek, G. Karpinski, C. Stiewe, P. Ziolkowski, C. Drasar, E. Muller, Potential-Seebeck-microprobe (PSM): measuring the spatial resolution of the Seebeck coefficient and the electric potential, 24th ICT IEEE (2005) 13-16.
[52] W. Liu, H. Chi, H. Sun, Q. Zhang, K. Yin, X. Tang, Q. Zhang, C. Uher, Advanced thermoelectrics governed by a single parabolic band: $Mg_2Si_{0.3}Sn_{0.7}$, a canonical example, Phys. Chem. Chem. Phys. 16 (2014) 6893-6897. https://doi.org/10.1039/C4CP00641K.
[53] Q. Zhang, L. Cheng, W. Liu, Y. Zheng, X. Su, H. Chi, H. Liu, Y. Yan, X. Tang, C. Uher, Low effective mass and carrier concentration optimization for high performance p-type $Mg_{2(1-x)}Li_{2x}Si_{0.3}Sn_{0.7}$ solid solutions, Phys. Chem. Chem. Phys. 16 (2014) 23576-23583. https://doi.org/10.1039/C4CP03468F.
[54] A.F. May, High-temperature transport in lanthanum telluride and other modern thermoelectric materials, California Institute of Technology, (2010).
[55] A.V. Krukau, O.A. Vydrov, A.F. Izmaylov, G.E. Scuseria, Influence of the exchange screening parameter on the performance of screened hybrid functionals, J. Chem. Phys. 125 (2006) 224106. https://doi.org/10.1063/1.2404663.
[56] G. Kresse, J. Furthmueller, Efficient iterative schemes for ab initio total-energy calculations using a plane-wave basis set, Phys. Rev. B 54 (1996) 11169. https://doi.org/10.1103/PhysRevB.54.11169.
[57] G. Kresse, D. Joubert, From ultrasoft pseudopotentials to the projector augmented-wave method, Physical Review B 59 (1999) 1758. https://doi.org/10.1103/PhysRevB.59.1758.
[58] S. Zhang, J.E. Northrup, Chemical potential dependence of defect formation energies in GaAs: Application to Ga self-diffusion, Phys. Rev. Lett. 67 (1991) 2339. https://doi.org/10.1103/PhysRevLett.67.2339.
[59] B. Ryu, M.-W. Oh, J.K. Lee, J.E. Lee, S.-J. Joo, B.-S. Kim, B.-K. Min, H.-W. Lee, S. Park, Defects responsible for abnormal n-type conductivity in Ag-excess doped PbTe thermoelectrics, J. Appl. Phys. 118 (2015) 015705. https://doi.org/10.1063/1.4923391.
[60] S.K. Bux, M.T. Yeung, E.S. Toberer, G.J. Snyder, R.B. Kaner, J.-P. Fleurial, Mechanochemical synthesis and thermoelectric properties of high quality magnesium silicide, J. Mater. Chem. 21 (2011) 12259-12266. https://doi.org/10.1039/C1JM10827A.
[61] W. Liu, H.S. Kim, S. Chen, Q. Jie, B. Lv, M. Yao, Z. Ren, C.P. Opeil, S. Wilson, C.-W. Chu, n-type thermoelectric material $Mg_2Sn_{0.75}Ge_{0.25}$ for high power generation, Proc. Natl. Acad. Scie. 112 (2015) 3269-3274. https://doi.org/10.1073/pnas.1424388112.
[62] L. Sudha, R. Sukumar, K. Uma Rao, Evaluation of activation energy (Ea) profiles of nanostructured alumina polycarbonate composite insulation materials, Int. J. Mater. Mech. Manuf. 2 (2014) 96-100. https://doi.org/10.7763/IJMMM.2014.V2.108.
[63] M. Mantina, Y. Wang, R. Arroyave, L. Chen, Z. Liu, C. Wolverton, First-principles calculation of self-diffusion coefficients, Phys. Rev. Lett. 100 (2008) 215901. https://doi.org/10.1103/PhysRevLett.100.215901.
[64] I.-H. Kim, $Mg_2B^{IV}$: Narrow Bandgap Thermoelectric Semiconductors, J. Korean Phys. Soc. 72 (2018) 1095-1109. https://doi.org/10.3938/jkps.72.1095.

[65] J.-H. Yang, W.-J. Yin, J.-S. Park, S.-H. Wei, Self-regulation of charged defect compensation and formation energy pinning in semiconductors, Scientific Reports 5 (2015) 16977. https://doi.org/10.1038/srep16977.
[66] G. Henkelman, H. Jónsson, Improved tangent estimate in the nudged elastic band method for finding minimum energy paths and saddle points, J. Chem. Phys 113 (2000) 9978-9985. https://doi.org/10.1063/1.1323224.
[67] G. Henkelman, B.P. Uberuaga, H. Jónsson, A climbing image nudged elastic band method for finding saddle points and minimum energy paths, J. Chem. Phys 113 (2000) 9901-9904. https://doi.org/10.1063/1.1329672.
[68] P. Gao, I. Berkun, R.D. Schmidt, M.F. Luzenski, X. Lu, P.B. Sarac, E.D. Case, T.P. Hogan, Transport and mechanical properties of high-ZT Mg2.08Si0.4-xSn0.6Sbx thermoelectric materials, J. Electron. Mater. 43 (2014) 1790-1803. https://doi.org/10.1007/s11664-013-2865-8.